

## ARTICLE TYPE

# Multiscale modeling of linear elastic heterogeneous structures based on a localized model order reduction approach

Philipp Diercks<sup>\*1,2</sup> | Karen Veroy<sup>2</sup> | Annika Robens-Radermacher<sup>1</sup> | Jörg F. Unger<sup>1</sup>

<sup>1</sup>Department 7.7 Modeling and Simulation, Bundesanstalt für Materialforschung und -prüfung (BAM), Unter den Eichen 87, 12205 Berlin, Germany

<sup>2</sup>Centre for Analysis, Scientific Computing and Applications (CASA) Department of Mathematics and Computer Science, University of Eindhoven, P.O. Box 513, 5600 MB Eindhoven, The Netherlands

## Correspondence

\*Philipp Diercks, Unter den Eichen 87, 12205 Berlin, Germany, Email: philipp.diercks@bam.de

## Present Address

Unter den Eichen 87, 12205 Berlin, Germany

## Abstract

In analyzing large scale structures it is necessary to take into account the fine scale heterogeneity for accurate failure prediction. Resolving fine scale features in the numerical model drastically increases the number of degrees of freedom, thus making full fine-scale simulations infeasible, especially in cases where the model needs to be evaluated many times.

In this paper, a methodology for fine scale modeling of large scale structures is proposed, which combines the variational multiscale method, domain decomposition and model order reduction. Addressing applications where the assumption of scale separation does not hold, the influence of the fine scale on the coarse scale is modelled directly by the use of an additive split of the displacement field. Possible coarse and fine scale solutions are exploited for a representative volume element (RVE) to construct local approximation spaces. The local spaces are designed such that local contributions of RVE subdomains can be coupled in a conforming way. Therefore, the resulting global system of equations takes the effect of the fine scale on the coarse scale into account, is sparse and reduced in size compared to the full order model. Several numerical experiments show the accuracy and efficiency of the method.

## KEYWORDS:

Multiscale methods; variational multiscale method; localized model order reduction; proper orthogonal decomposition; domain decomposition methods

## 1 | INTRODUCTION

Many problems in science and engineering involve multiple scales. With large disparities present in spatial or temporal scales, it is often insufficient to assume a homogeneous material in the analysis of a mechanical structure. For example, the dispersed phases (particles or fibers) in a composite material may lead to fluctuations in the displacement field which cannot be captured by

the phenomenological macroscale model. Therefore, in analyzing large scale structures, it is often necessary to take into account the materials' fine scale heterogeneity to more accurately model the structure's behaviour. However, capturing the underlying physical phenomena, e. g. , the formation of macrocracks, by resolving the fine scales in the numerical model also leads to a significant increase in the computational cost. While parallel computing mitigates this issue, the size of the discrete equation system remains and thus the computational effort of the direct numerical simulation poses a major problem, particularly in applications requiring repeated evaluations of the model.

It is often sufficient to predict macroscopic properties of the multiscale system based on a representative volume element (RVE), i. e. the smallest volume, such that the material with discontinuous structures can be statistically homogeneous and the variation of the macroscopic variables is negligibly small. This way, to consider the small-scale effect on the large scale, resolving the small-scale features in the entire domain is not required. However, this approach rests on the assumption of separation of scales and consequently the existence of an RVE.

The present paper addresses applications where the assumption of separation of scales does not hold. A superposition-based ansatz is used to model the nonlocal influence of the fine scale on the coarse scale directly. Furthermore, by means of model order reduction techniques, the dimension of the discrete system of equations is reduced and the computational cost to solve the discretized problem.

In the context of multiscale methods in computational mechanics, computational homogenization approaches, such as the FE<sup>2</sup> method (see e. g. <sup>1,2,3,4</sup>) are widely used. The nested solution process, where for each material point on the coarse scale a fine scale boundary value problem based on an RVE is solved to obtain the homogenized macroscopic response, is still a computationally demanding task. Moreover, separation of scales can only be assumed if the macroscopic dimensions are significantly larger than the dimensions of the micro-scale features<sup>5</sup>. Relying on this assumption, an RVE can be defined which must, on average, be typical for the heterogeneous material, but also small in dimension compared to the entire body of the structure. A more precise definition is given by Bishop and Hill<sup>6</sup> and later work by Hill<sup>7</sup>, where the concept of an RVE was introduced under the label *unit cube*. Furthermore, the existence and size of an RVE is analyzed by Gitman et al.<sup>8,9</sup>, and it is shown that, in the presence of macroscopic cracks emerged from the localization of microdefects, a useful RVE cannot be found.

To reduce the computational cost of numerical methods in many-query contexts involving parameterized partial differential equations (pPDEs), i. e. , where the same problem has to be solved for different parameter values many times, or where real-time performance is required, projection-based model order reduction techniques have gained great popularity (see the textbooks<sup>10,11</sup> for an introduction to the topic). The high dimensional numerical problem (high-fidelity approximation or full order model (FOM)) is replaced by a reduced order model (ROM) of small dimension, which is achieved by the projection of the original system of equations upon a subspace of the solution manifold. A key point is the construction of the reduced basis, which spans the low dimensional subspace, from a set of suitably selected high-fidelity solutions. In (now standard) reduced basis

(RB) methods, the so-called snapshots are selected via the weak greedy algorithm<sup>12,13</sup>. Another popular method for subspace construction is the proper orthogonal decomposition (POD). Here, the snapshots are gathered column-wise in a matrix and the reduced basis is computed as the left singular vectors associated with the largest singular values of this matrix. For a review, see for example the book by Holmes et al.<sup>14</sup> and the work by Kunisch and Volkwein<sup>15</sup> for applications to partial differential equations. A general challenge with POD is the selection of the snapshots. Usually, the parameter space has to be densely sampled and the resulting reduced basis is not guaranteed to accurately approximate solutions outside the chosen training set. However, neither of the above approaches yield an efficient reduction of nonlinear problems. Due to the repeated evaluation of the weak form over the full domain (e. g. assembly of the stiffness matrix and internal force vector), the reduced system still depends on the high dimension of the FOM. Among others, well-known techniques to address this issue are the Empirical Interpolation Method (EIM)<sup>16</sup> and its discrete variant<sup>17</sup> or the Hyper-Reduction<sup>18,19</sup>. Moreover, the more recent approaches<sup>20,21</sup> make use of machine learning methods to construct ROMs for nonlinear problems.

The contributions<sup>22,23,24</sup> combine the  $FE^2$  approach with model reduction of the fine scale problem to address the issue of computational complexity.

Regardless of this, in cases where the assumption of separation of scales as the basis of classical homogenization approaches does not hold, full fine scale simulations become inevitable. In this case, however, limitations of the established model order reduction techniques become apparent; examples of such limitations include prohibitively large reduced spaces due to high dimensional parameter spaces or computationally expensive offline phases due to large computational domains.

To alleviate these shortcomings, methods combining multiscale methods, domain decomposition and model order reduction were developed. Approaches of this kind are known as *localized model order reduction methods*, and an extensive review is given by Buhr et al.<sup>25</sup>. The main idea is the construction of local reduced spaces on subdomains, i. e. parts of the global domain, which are then coupled (either in a conforming or non-conforming way) to obtain a global approximation. Local reduced spaces that are optimal in the sense of Kolmogorov can be constructed by solution of a transfer eigenvalue problem<sup>26,27</sup>, which also uses the concept of oversampling first introduced in the context of the multiscale finite element method (MsFEM)<sup>28</sup>. Although the direct computation of the singular values of this transfer operator is computationally very expensive, Buhr and Smetana<sup>29</sup> show for the non-parametric case that the associated transfer operator can be well approximated by random sampling. The authors note that the approach can be extended to the parameter-dependent case in a straightforward manner<sup>27,30</sup>. In addition, the variational multiscale method (VMM) was introduced as a general “procedure for deriving models and numerical methods capable of dealing with multiscale phenomena ubiquitous in science and engineering”<sup>31</sup>. Its close relation to the MsFEM is discussed in the context of mixed finite element methods<sup>32</sup>. Belonging to the class of superposition-based multiscale methods (see<sup>33</sup> for an overview), it is a natural choice for problems in computational mechanics.

The aim of the present paper is to enable full mesoscale simulations of large scale structures. While this contribution is limited to the linear case, in the long run it is necessary to fully resolve the fine scales in the numerical model to include localization phenomena and nonlinear material behaviour. This necessitates the direct modeling of the nonlocal effect of the fine scale on the coarse scale, which is achieved by an additive split of the displacement field in coarse and fine scale parts, as in the VMM. Both coarse and fine scale parts are approximated by finite elements which automatically introduce a domain decomposition character, with coarse grid cells being equivalent to subdomains. The problem of computational complexity is addressed by the construction of local reduced basis functions for the coarse and fine scale parts. While the coarse scale basis functions are defined a priori, POD is used to construct the basis for the fine scale. For the selection of the snapshots, in view of the extension of the method to the nonlinear case, the solution of the transfer eigenvalue or equivalent oversampling problem with physically meaningful instead of random boundary conditions is proposed. Furthermore, in order to derive practical methods in the framework of the VMM, it is usually necessary to impose additional constraints on the fine scale to eliminate it from the coarse scale equation. In the simplest case, the fine scale part is assumed to vanish on coarse grid cell boundaries. Other, physically more sound ideas leading to a Lagrange type method are discussed by Hund and Ramm<sup>34</sup>. In this contribution, the fine scale term is further decomposed (see section 3.3), enabling a direct coupling of adjacent subdomains and ensuring continuity of the displacements without requiring the fine scale solution to vanish along the edges of the coarse grid.

The proposed method to model linear elastic heterogeneous structures is described as follows. First, in section 2, the problem setting and formal procedure of the method are described. Section 3 deals with the construction of local approximation spaces. Numerical examples illustrating the performance of the suggested approach are discussed in section 4. The conclusion and an outlook are given in section 5.

## 2 | PROBLEM SETTING AND MODELING

While the method could be applied to other partial differential equations, only the balance of linear momentum in the static case on a large computational domain  $\Omega_{\text{gl}} \subset \mathbb{R}^d$  (the suffix ‘gl’ stands for global) is considered, with boundary  $\partial\Omega_{\text{gl}} = \Sigma_{\text{N}} \cup \Sigma_{\text{D}}$ , where  $\Sigma_{\text{N}}$  and  $\Sigma_{\text{D}}$  denote Neumann and Dirichlet boundaries, respectively, and  $d = 2, 3$  is the spatial dimension. Without loss of generality, volumetric forces are neglected, and the displacement solution  $\mathbf{u}_{\text{gl}}$  is sought such that

$$\begin{aligned} -\nabla \cdot \boldsymbol{\sigma}(\nabla \mathbf{u}_{\text{gl}}) &= 0 \quad \text{in } \Omega_{\text{gl}}, \\ \boldsymbol{\sigma}(\nabla \mathbf{u}_{\text{gl}}) \cdot \mathbf{n} &= \hat{\mathbf{t}} \quad \text{on } \Sigma_{\text{N}}, \\ \mathbf{u}_{\text{gl}} &= \hat{\mathbf{u}} \quad \text{on } \Sigma_{\text{D}}. \end{aligned} \tag{1}$$

Here the Cauchy stress tensor  $\boldsymbol{\sigma}$  for one of the  $M$  components of the heterogeneous linear elastic material is given by

$$\boldsymbol{\sigma}_m = \lambda_m^1 (\boldsymbol{\varepsilon}(\mathbf{u}_{\text{gl}}) \cdot \cdot \mathbb{1}) \mathbb{1} + 2\lambda_m^2 \boldsymbol{\varepsilon}(\mathbf{u}_{\text{gl}}), \quad \text{with } m = 1, \dots, M, \quad (2)$$

where  $\lambda_m^1$  and  $\lambda_m^2$  are Lamé's constants. The linear strain operator is denoted by  $\boldsymbol{\varepsilon}(\mathbf{v}) = \frac{1}{2} (\nabla \mathbf{v} + \nabla \mathbf{v}^T)$ . Moreover,  $\mathbf{n}$  is the body's surface outward normal vector,  $\hat{\mathbf{t}}$  is the traction given on the Neumann boundary  $\Sigma_N$  and  $\hat{\mathbf{u}}$  is the displacement prescribed on the Dirichlet boundary  $\Sigma_D$ . Introducing a Hilbert space  $\mathbb{V}_{\text{gl}}$ , the weak form for eq. (1) reads:

$$a(\mathbf{u}_{\text{gl}}, \mathbf{v}) = f(\mathbf{v}), \quad \forall \mathbf{v} \in \mathbb{V}_{\text{gl}}, \quad (3)$$

where

$$a(\mathbf{w}, \mathbf{v}) = \sum_{m=1}^M \int_{\Omega_{\text{gl}}^m} \lambda_m^1 \text{tr}(\boldsymbol{\varepsilon}(\mathbf{w})) \text{tr}(\boldsymbol{\varepsilon}(\mathbf{v})) + 2\lambda_m^2 \boldsymbol{\varepsilon}(\mathbf{w}) \cdot \cdot \boldsymbol{\varepsilon}(\mathbf{v}) \, dV \quad (4)$$

and

$$f(\mathbf{v}) = \int_{\partial\Omega_{\text{gl}}} \hat{\mathbf{t}} \cdot \mathbf{v} \, dA. \quad (5)$$

Here,  $\text{tr}(\bullet)$  denotes the trace of a tensor and ' $\cdot \cdot$ ' stands for the scalar product of two 2nd-order tensors (2-fold contraction as defined in section 2.1.15 of<sup>35</sup>). The energy inner product and energy norm are defined as

$$(\mathbf{w}, \mathbf{v})_{\mathbb{V}_{\text{gl}}} = a(\mathbf{w}, \mathbf{v}), \quad \forall \mathbf{w}, \mathbf{v} \in \mathbb{V}_{\text{gl}}, \quad (6)$$

$$\|\mathbf{v}\|_{\mathbb{V}_{\text{gl}}}^2 = a(\mathbf{v}, \mathbf{v}), \quad \forall \mathbf{v} \in \mathbb{V}_{\text{gl}}. \quad (7)$$

## 2.1 | Full order model

The *direct numerical solution* or *full order model* is defined as the finite element approximation of eq. (3), searching for the solution in a discrete space  $\mathbb{V}_{\delta} \subset \mathbb{V}_{\text{gl}}$  (of high fidelity; suffix  $\delta$ ): find  $\mathbf{u}_{\delta} \in \mathbb{V}_{\delta}$ , such that

$$a(\mathbf{u}_{\delta}, \mathbf{v}) = f(\mathbf{v}), \quad \forall \mathbf{v} \in \mathbb{V}_{\delta}. \quad (8)$$

The dimension of the discrete space is denoted by  $N_{\delta} = \dim(\mathbb{V}_{\delta})$ , and by equipping  $\mathbb{V}_{\delta}$  with a standard finite element basis  $\{\phi_i\}_{i=1}^{N_{\delta}}$ , the stiffness matrix and right hand side can be written as

$$(\mathbf{A}_{\delta})_{ij} = a(\phi_j, \phi_i), \quad (\mathbf{f}_{\delta})_i = f(\phi_i). \quad (9)$$

## 2.2 | Multiscale method

Every material is intrinsically multiscale. In the framework of continuum mechanics, often the assumption of a homogeneous material to solve macroscale problems is sufficient. However, it is only a homogenized approximation of the underlying finer

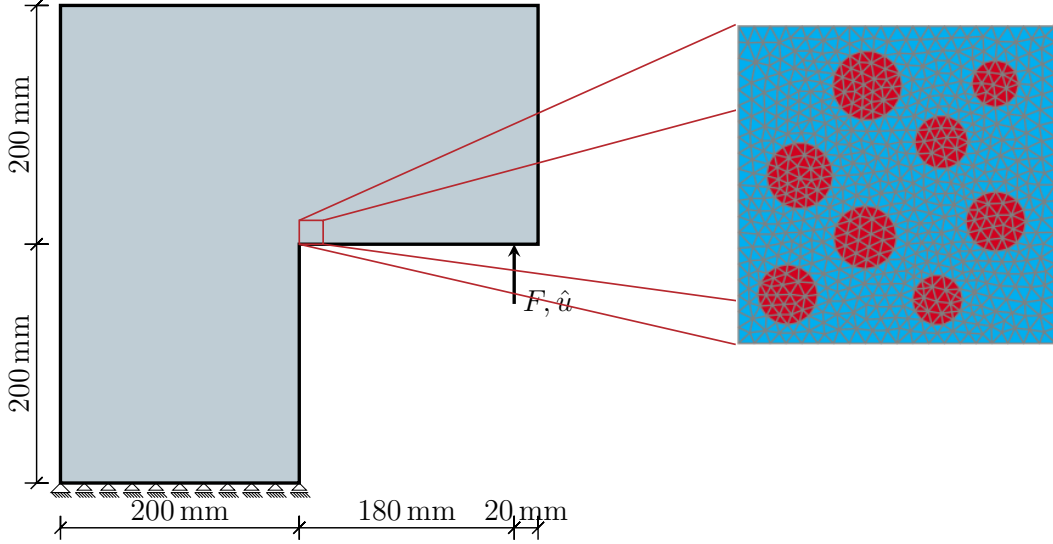


**FIGURE 1** L-shaped panel test specimen and exemplary fine scale structure (RVE).

scales and thus not suitable in loading conditions where the real physical phenomena on the fine scale greatly influence the macroscopic behaviour. Consider for example the propagation of a crack in the test specimen shown in fig. 1, which is only tractable by resolving the fine scale in the numerical model. The macroscopic approximation then needs to be improved by fine scale functions taking into account fluctuations in the displacement field due to the heterogeneous fine scale structure. Note that the discretization of the fine scale structure (RVE) is assumed to be the same throughout the whole mesoscale structure and that it is aimed at a reduction of the fully dissolved RVE subdomain by construction of coarse grid elements which are able to model both scales sufficiently. Following this line of thought, an additive split of the displacement solution

$$\mathbf{u}_{\text{gl}} = \mathbf{u}_c + \mathbf{u}_f, \quad \mathbb{V}_{\text{gl}} = \mathbb{V}_c \oplus \mathbb{V}_f \quad (10)$$

is introduced, such that

$$a(\mathbf{u}_c, \mathbf{v}_c) + a(\mathbf{u}_f, \mathbf{v}_c) = f(\mathbf{v}_c) \quad \forall \mathbf{v}_c \in \mathbb{V}_c, \quad (11)$$

$$a(\mathbf{u}_c, \mathbf{v}_f) + a(\mathbf{u}_f, \mathbf{v}_f) = f(\mathbf{v}_f) \quad \forall \mathbf{v}_f \in \mathbb{V}_f. \quad (12)$$

Here  $(\bullet)_c$  denotes the coarse scale part and  $(\bullet)_f$  the fine scale part. The corresponding discrete spaces are associated with coarse scale and fine scale partitions of the domain  $\Omega_{\text{gl}}$  as depicted in fig. 2. It is assumed that an RVE for the analyzed heterogeneous material exists and that the global domain can be decomposed into  $N_c$  non-overlapping RVE subdomains denoted by  $\Omega_i$ ,  $i = 1, 2, \dots, N_c$ . The subdomain boundaries are denoted by  $\Gamma_e^i$ , with  $e = 1, 2, 3, 4$  referring to the respective bottom, right, top and left

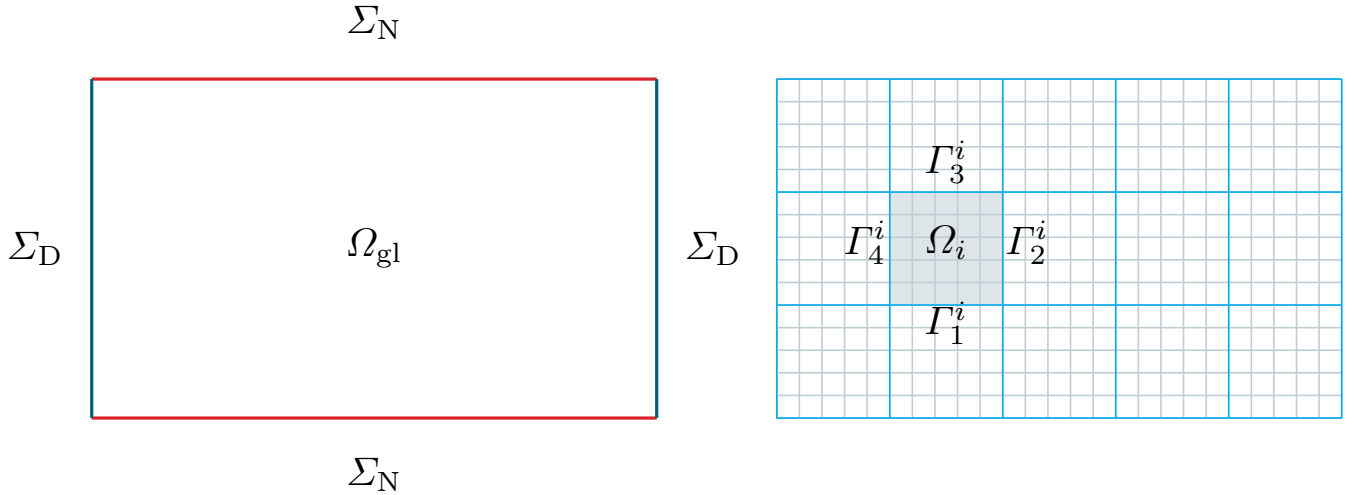


**FIGURE 2** Exemplary computational domain  $\Omega_{\text{gl}}$  on the left and coarse scale (blue) and fine scale (gray) grid partition on the right. A subdomain  $\Omega_i$  and its edges  $\Gamma_e^i$  are also shown.

edge of the subdomain. Analogously, the global space is decomposed into subdomain spaces  $\mathbb{V}_i$  with dimension  $n_\delta = \dim(\mathbb{V}_i)$ ,

$$\mathbb{V}_{\text{gl}} = \bigoplus_{i=1}^{N_c} \mathbb{V}_i. \quad (13)$$

Section 3 deals with the construction of reduced basis functions which yield a good approximation of  $\mathbf{u}_{\text{gl}}$ , such that the PDE eq. (1) is locally fulfilled on  $\Omega_i$ . The proposed approach features a local basis  $\{\xi_k\}_{k=1}^n = \{\varphi_i\}_{i=1}^{n_c} \cup \{\psi_j\}_{j=1}^{n_f}$ , with  $n$  being the maximum number of basis functions, which has partition of unity property on vertices of the coarse grid and is conforming on subdomain boundaries  $\Gamma_e^i$ . Here  $\varphi_i$  and  $\psi_j$  are the  $n_c$  coarse scale and  $n_f$  fine scale functions, respectively. The reduced basis can be expressed in the standard finite element basis  $\phi_j$  associated with the fine grid

$$\xi_k = \sum_{j=1}^{n_\delta} \mathbf{B}_{jk} \phi_j, \quad (14)$$

where the  $k$ -th column of the matrix  $\mathbf{B} \in \mathbb{R}^{n_\delta \times n}$  holds the coefficients of the  $k$ -th basis function. The local contribution of a subdomain is then given by

$$\mathbf{A}_n = \mathbf{B}^T \mathbf{A}_\delta^{\text{loc}} \mathbf{B}, \quad \mathbf{f}_n = \mathbf{B}^T \mathbf{f}_\delta^{\text{loc}}, \quad (15)$$

where  $\mathbf{A}_\delta^{\text{loc}} \in \mathbb{R}^{n_\delta \times n_\delta}$  and  $\mathbf{f}_\delta^{\text{loc}} \in \mathbb{R}^{n_\delta}$  denote the stiffness matrix and external force vector, respectively, of an RVE subdomain. Note that unless body forces are present,  $\mathbf{f}_\delta^{\text{loc}}$  is zero in case  $\Gamma_e^i \cap \Sigma_N = \emptyset$  or  $\hat{\mathbf{t}} = \mathbf{0}$  which is the case for most subdomains. Due to the above-mentioned properties of the reduced basis functions, the local contributions  $\mathbf{A}_n \in \mathbb{R}^{n \times n}$  and  $\mathbf{f}_n \in \mathbb{R}^n$  can be sorted into global vectors following the usual assembly procedure of a quadrilateral (or hexahedral) finite element, where each node, edge and face (3D) is associated with a fixed number of degrees of freedom (DoFs). The global system of the *reduced order*

model of size  $N \ll N_\delta$  is then written as

$$\mathbf{A}_N \mathbf{u}_N = \mathbf{f}_N, \quad (16)$$

where  $\mathbf{A}_N \in \mathbb{R}^{N \times N}$ ,  $\mathbf{f}_N \in \mathbb{R}^N$  and  $N$  is the number of unknown DoFs in the reduced order model.

### 3 | CONSTRUCTION OF LOCAL APPROXIMATION SPACES

In this section, the construction of the reduced basis functions for the coarse scale  $\{\boldsymbol{\varphi}_i\}_{i=1}^{n_c}$  and the reduced basis functions for the fine scale  $\{\boldsymbol{\psi}_i\}_{i=1}^{n_f}$  is addressed. The proposed *offline phase* consists of three stages:

1. direct calculation of coarse-scale basis  $\{\boldsymbol{\varphi}_i\}_{i=1}^{n_c}$ ,
2. calculation of fine-scale edge basis functions  $\{\boldsymbol{\chi}_i^e\}_{i=1}^{n_{\text{mpe}}}$ , where  $n_{\text{mpe}}$  denotes the number of modes per (subdomain) edge; via two approaches:
  - (a) by solving an oversampling problem (leading to an *empirical* basis),
  - (b) by constructing *hierarchical* finite element shape functions (see e. g. chapter 8 in <sup>36</sup>),
3. calculation of subdomain basis functions  $\{\boldsymbol{\psi}_i\}_{i=1}^{n_f}$  from  $\{\boldsymbol{\chi}_i^e\}_{i=1}^{n_{\text{mpe}}}$ .

#### 3.1 | Direct calculation of coarse scale basis

The coarse scale basis is required to form a partition of unity on the subdomain boundary  $\partial\Omega_i$ , to enable the assembly procedure described in section 2. Therefore, standard finite element shape functions on the boundary of the subdomain are extended into the interior by solving the variational problem on the RVE subdomain. The coarse scale basis functions are defined as the solution of

$$a(\boldsymbol{\varphi}_j, \mathbf{v}) = 0, \quad \boldsymbol{\varphi}_j = N_j \text{ on } \partial\Omega_i, \quad \forall \mathbf{v} \in \mathbb{V}_i, \quad (17)$$

where

$$a(\mathbf{w}, \mathbf{v}) = \sum_{m=1}^M \int_{\Omega_i^m} \lambda_m^1 \text{tr}(\boldsymbol{\varepsilon}(\mathbf{w})) \text{tr}(\boldsymbol{\varepsilon}(\mathbf{v})) + 2\lambda_m^2 \boldsymbol{\varepsilon}(\mathbf{w}) \cdot \cdot \boldsymbol{\varepsilon}(\mathbf{v}) \, dV \quad (18)$$

and  $N_j$  being the standard Lagrange basis functions. For quadrilateral coarse-grid cells and linear interpolation of the coarse-scale, this yields a coarse-scale basis of size  $n_c = 8$ .



### 3.2 | Calculation of fine scale edge basis functions

As mentioned in the beginning of section 3, two different approaches are considered. The fine scale edge basis functions may be defined as *hierarchical* shape functions a priori. In this case, no precomputation is required and one could directly compute the extension of the edge basis into the interior of the subdomain, as described in section 3.3. The construction of the *empirical* fine scale edge basis poses the main challenge in the proposed framework. In order to exploit fine scale solutions of the PDE eq. (1) on any subdomain  $\Omega_i$ , we make use of the concept of oversampling<sup>28</sup>. First, the oversampling domain  $\hat{\Omega}$  is defined, such that  $\Omega_i \subsetneq \hat{\Omega} \subset \Omega_{\text{gl}}$ . Furthermore, the distance between the boundary  $\partial\Omega_i$  and  $\Gamma_\mu := \partial\hat{\Omega} \setminus \partial\Omega_{\text{gl}}$  is greater than zero, i. e.  $\text{dist}(\Gamma_\mu, \partial\Omega_i) \geq \rho > 0$ . Dependent on the configuration for a particular  $\Omega_i$ ,  $\Gamma_N := \partial\hat{\Omega} \cap \Sigma_N$  or  $\Gamma_D := \partial\hat{\Omega} \cap \Sigma_D$  may be not empty and Neumann or Dirichlet boundary conditions of the global problem need to be considered in the oversampling as well. The challenge in solving eq. (1) on  $\hat{\Omega}$  lies in the definition of the boundary data on  $\Gamma_\mu$  which is used to exploit possible solutions of the PDE on  $\Omega_i$  and therefore can be regarded as a parameter  $\mu \in \mathbb{P}$ . Numerically, the maximum size of the parameter space  $\mathbb{P}$  is the number of degrees of freedom on  $\Gamma_\mu$ . Consider for example  $\hat{\Omega}$  as a  $3 \times 3$  block of RVEs with a single aggregate, as shown in fig. 5a. The RVE is discretized with 11 vertices per edge, leading to 120 vertices on  $\Gamma_\mu$ . For linear triangular elements, this would lead to a parameter space  $\mathbb{P} = \mathbb{R}^{240}$ , where a dense uniform sampling as usually done in standard greedy approaches as introduced in<sup>13</sup> is infeasible. For this reason by simply choosing the boundary data as

$$\mathbf{g}(\mu) = \sum_{i=1}^P N_i \mu_i, \quad (19)$$

the parameter space is reduced to  $\mathbb{P} = \mathbb{R}^P$ . The shape functions  $N_i$  are chosen as standard finite element shape functions defined on the oversampling domain  $\hat{\Omega}$ , either of Lagrange or ‘serendipity’ (see e. g. chapter 8 in<sup>36</sup>) type. The DoFs in this *load parametrization* are the components  $\mu_i \in \mathbb{R}$  of the parameter value  $\mu = (\mu_1, \mu_2, \dots, \mu_P)$ . The *oversampling problem* is then given as

$$\begin{aligned} -\nabla \cdot \boldsymbol{\sigma}(\nabla \mathbf{u}(\mu)) &= 0 \quad \text{in } \hat{\Omega}, \\ \boldsymbol{\sigma}(\nabla \mathbf{u}(\mu)) \cdot \mathbf{n} &= \hat{\mathbf{t}} \quad \text{on } \Gamma_N, \\ \mathbf{u}(\mu) &= \hat{\mathbf{u}} \quad \text{on } \Gamma_D, \\ \mathbf{u}(\mu) &= \mathbf{g}(\mu) \quad \text{on } \Gamma_\mu. \end{aligned} \quad (20)$$

Besides the reduction of the parameter space, the *load parametrization* eq. (19) also enables including physical states of the structure of interest in the training. The choice of a training set  $\mathbb{P}_h$ , a finite number of points in  $\mathbb{P}$ , is discussed in section 3.4 while for the rest of this subsection it is assumed that a suitable training set exists.

As an example, fig. 3 shows the oversampling domain  $\hat{\Omega}$  for a subdomain of interest  $\Omega_i$  that is entirely inside the structure and the DoFs in the *load parametrization* for serendipity shape functions, i. e.  $P = 16$ .

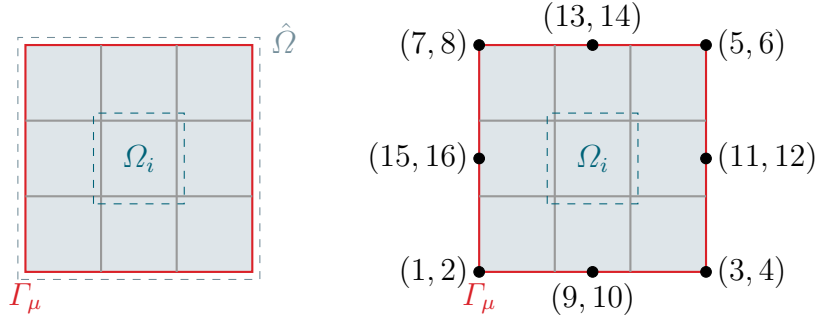


**FIGURE 3** Oversampling domain  $\hat{\Omega}$ , RVE domain  $\Omega_i$ , and indices of the degrees of freedom of the load parametrization.

For constructing the fine scale edge basis, we proceed as follows. For any parameter  $\mu \in \mathbb{P}_h$ , the oversampling problem eq. (20) is solved and the solution is restricted to the domain of interest, which is denoted by  $\mathbf{u}(\mu)|_{\Omega_i}$ . The coarse scale DoFs are the total displacement values at vertices of the coarse grid and the fine scale part is obtained by subtracting the coarse scale part. The fine scale part is further restricted to the solution on the edges  $\mathbf{u}_f(\mu)|_{\Gamma_e^i}$ . This way, four fine scale edge snapshots are obtained for each parameter value  $\mu$  and gathered in *snapshot sets* for edges opposite to each other, where a continuous coupling needs to be ensured. For example, a bottom-top-set and a right-left-set is defined for RVEs inside the structure (leading to a *delta* training set of cardinality  $2P$ ; see section 3.4 for its definition), while depending on the configuration, not all edge snapshots are relevant or it is necessary to additionally take snapshots from neighbouring configurations into account. Since the different configurations are problem specific, this is discussed in more detail in section 4.2.

Finally, the edge snapshots are gathered column-wise in a so-called *snapshot matrix* and POD is applied to compute the fine scale edge basis. It is noted that the POD algorithm<sup>37</sup> used in this paper computes the POD modes via the *method of snapshots*<sup>38</sup> which is summarized briefly in the paragraph below. The fine scale edge basis is denoted as  $\{\chi_j^e\}_{j=1}^{n_{\text{mpe}}}$ , with  $e = 1, 2, 3, 4$  referring to one of the edges of the RVE domain  $\Gamma_e^i$  and  $n_{\text{mpe}}$  denoting the number of modes per edge. Note that for subdomains inside the structure, the sets  $\{\chi_j^1\}_{j=1}^{n_{\text{mpe}}}$  (bottom) and  $\{\chi_j^3\}_{j=1}^{n_{\text{mpe}}}$  (top) and analogously the sets  $\{\chi_j^2\}_{j=1}^{n_{\text{mpe}}}$  (right) and  $\{\chi_j^4\}_{j=1}^{n_{\text{mpe}}}$  (left) are identical.

### Proper orthogonal decomposition

Given a set of  $N_{\text{samples}}$  snapshots  $\{s_i\}_{i=1}^{N_{\text{samples}}}$  the snapshot matrix  $\mathbf{S} \in \mathbb{R}^{S \times N_{\text{samples}}}$  is defined as

$$\mathbf{S} = [s_1, s_2, \dots, s_{N_{\text{samples}}}] . \quad (21)$$

In general the snapshots can be vectors in a Hilbert space  $\mathbb{V}$  with dimension  $S = \dim(\mathbb{V})$ . Next, the correlation matrix  $\mathbf{C} \in \mathbb{R}^{N_{\text{samples}} \times N_{\text{samples}}}$  is formed by the Gramian of the set of snapshots

$$C_{ij} = (s_i, s_j)_{\mathbb{V}} , \quad i, j = 1, 2, \dots, N_{\text{samples}} . \quad (22)$$

Then, the eigenvalue decomposition of the correlation matrix, with eigenvalues  $\lambda_k$  and eigenvectors  $\mathbf{v}_k$ ,  $k = 1, 2, \dots, \min(n_{\text{modes}}, N_{\text{samples}})$ , is computed. Depending on the implementation, the number of POD modes  $n_{\text{modes}}$  can be specified directly by the user or in terms of a tolerance on the eigenvalues. The  $k$ -th POD mode  $\chi_k$  is finally obtained by

$$\chi_k = \frac{1}{\sqrt{\lambda_k}} \mathbf{S} \mathbf{v}_k. \quad (23)$$

### 3.3 | Calculation of subdomain basis functions

The final step in constructing the reduced basis for the fine scale part of the displacement solution consists in the extension of the POD edge modes into the RVE domain  $\Omega_i$ . It is important to note that, by setting the same function on a single edge for adjacent RVEs, continuity between adjacent subdomains is ensured. Furthermore, to enable the standard assembly procedure as in the finite element method, it is necessary to enforce zero boundary conditions on edges  $\partial\Omega_i \setminus \Gamma_e^i$  where the POD mode is not prescribed. For each edge  $\Gamma_e^i$ , with  $e = 1, 2, 3, 4$ , and each POD mode in the set  $\{\chi_j^e\}_{j=1}^{n_{\text{mpe}}}$ , find  $\psi_j^e$  such that

$$a(\psi_j^e, \mathbf{v}) = 0, \quad \forall \mathbf{v} \in \mathbb{V}_i, \quad (24)$$

$$\text{with } \psi_j^e = \chi_j^e \text{ on } \Gamma_e^i \text{ and } \psi_j^e = \mathbf{0} \text{ on } \partial\Omega_i \setminus \Gamma_e^i,$$

where the bilinear form  $a(\cdot, \cdot)$  is given by eq. (18). Note that, for example, the sets  $\{\chi_j^1\}_{j=1}^{n_{\text{mpe}}}$  (bottom) and  $\{\chi_j^3\}_{j=1}^{n_{\text{mpe}}}$  (top) are identical, while this is not the case for  $\{\psi_j^1\}_{j=1}^{n_{\text{mpe}}}$  (bottom) and  $\{\psi_j^3\}_{j=1}^{n_{\text{mpe}}}$  (top). All  $n_f = 4n_{\text{mpe}}$  solutions of eq. (24) are then gathered in one set of fine scale basis functions

$$\{\psi_j\}_{j=1}^{n_f} = \{\psi_k^1\}_{k=1}^{n_{\text{mpe}}} \cup \{\psi_k^2\}_{k=1}^{n_{\text{mpe}}} \cup \{\psi_k^3\}_{k=1}^{n_{\text{mpe}}} \cup \{\psi_k^4\}_{k=1}^{n_{\text{mpe}}}. \quad (25)$$

### 3.4 | Training sets

In this section, two different choices for the training set which are studied in the numerical examples (section 4) are discussed. For the first training set (referred to as *delta*), the parameters  $\mu \in \mathbb{P} = \mathbb{R}^P$  are chosen as coefficients of the unit vectors  $\{\mathbf{e}_i : 1 \leq i \leq P\}$  of  $\mathbb{R}^P$ . This way the DoFs in the load parametrization of the oversampling problem are excited separately and this leads to a training set of size  $P$ .

The choice for the second training set is related to the particular choice of load parametrization in the oversampling problem, in which it is assumed that the macroscopic response in most applications is well approximated by quadratic polynomials. Another motivation for this choice is the possibility to include physical states that are actually present in the *structure of interest (SoI)* and hence it is referred to as the *SoI* training set. To this end, prior to the solution of the oversampling problem, a standard FE problem with homogenized material parameters is solved on the coarse grid. The parameter values of the training set are then given by DoFs local to each coarse grid cell, i. e. quadrilaterals with quadratic shape functions in this case. Thus, the training set is of

the size of the number of coarse grid cells  $N_c$  and, in analogy to the different configurations of oversampling problems present in the structure, it is divided into several training sets used to compute the snapshots in each of the oversampling problems. However, this also poses the problem that the training data for subdomains  $\Omega_i$ , with  $\partial\Omega_i \cap \partial\Omega_{gl} \neq \emptyset$ , is sparse. This may lead to only a few basis functions and large approximation errors for these particular subdomains. Therefore, in this contribution the approach is limited in the sense that the *SoI* basis needs to be extended by *delta* modes.

## 4 | NUMERICAL EXPERIMENTS

In this section, the performance of the suggested empirical basis for different training sets is studied and compared to the hierarchical basis as a naïve choice for the approximation of the fine scale part. Section 4.1 shows (empirically) the exponential decay of the local projection error for a random testing set within the chosen parametrization (eq. (19)). In the presented block example, the local projection error carries over to the global approximation if the Dirichlet data lies in the span of the reduced basis. In section 4.2 a beam under the state of pure bending is analyzed for varying ratio of the elastic moduli as a measure for the heterogeneity and the empirical basis' performance is shown to be superior to that of the hierarchical basis for ratios greater than one. The applicability of the method to more complex problems is demonstrated by the example of an L-shaped panel in section 4.3. If not stated otherwise, the material parameters listed in table 1 are used. Triangle elements with quadratic shape functions are used for the fine grid discretization of the RVE types used in the examples. Figure 4 shows the results of the mesh convergence analysis carried out. For different levels of refinement eq. (3) is solved on the RVE domain with boundary data given by eq. (29) and the error relative to a reference solution computed on the finest mesh is measured in the energy norm. The mesh is regarded as converged if the relative error in the energy norm is below one percent which leads to the partitions as shown in fig. 5. In all examples, the global error relative to the *full order model* (eq. (3)) is computed as follows. The absolute error on subdomain  $\Omega_i$  defined as  $e_i = (\mathbf{u}_{\text{fom}})_i - (\mathbf{u}_{\text{rom}})_i$  is measured in the energy norm as

$$\|e_i\|_{V_i}^2 = a(e_i, e_i). \quad (26)$$

The global absolute error is thus given by the square root of the sum of the local norm squared

$$\|e\|_{V_{gl}} = \sqrt{\sum_{i=1}^{N_c} \|e_i\|_{V_i}^2}. \quad (27)$$

Analogously, the global relative error is given by

$$\frac{\|e\|_{V_{gl}}}{\|\mathbf{u}_{\text{fom}}\|_{V_{gl}}} = \frac{\sqrt{\sum_{i=1}^{N_c} \|e_i\|_{V_i}^2}}{\sqrt{\sum_{i=1}^{N_c} \|(\mathbf{u}_{\text{fom}})_i\|_{V_i}^2}}. \quad (28)$$

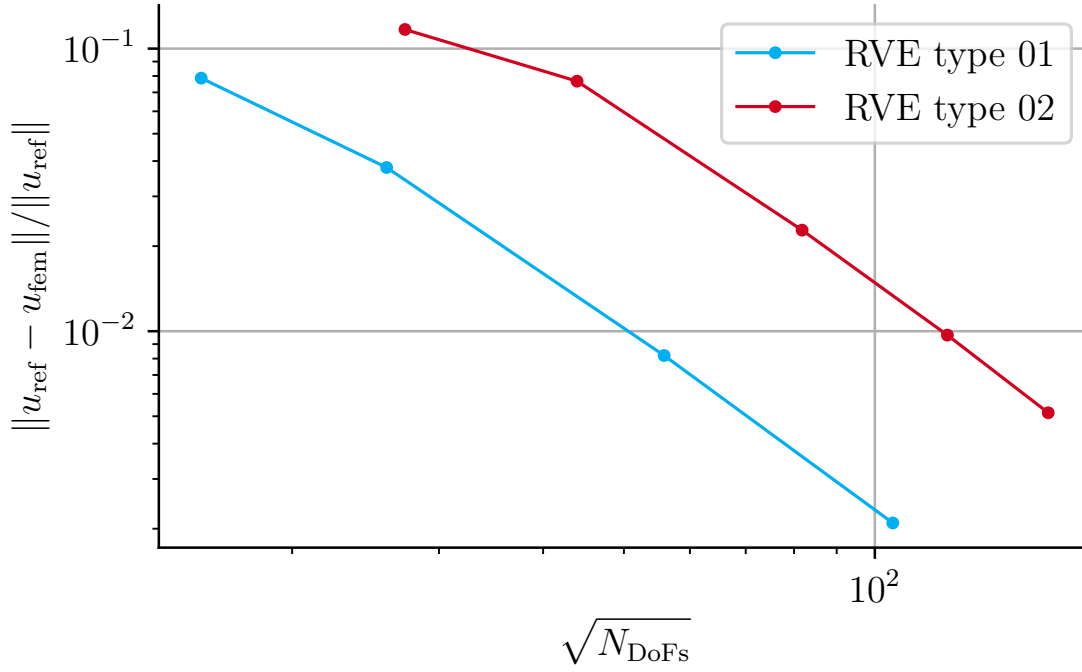


**FIGURE 4** Relative error in the energy norm against square root of number of degrees of freedom in the mesh convergence analysis.

**TABLE 1** Material parameters (taken from table 4 in<sup>39</sup>).

	Mortar matrix	Aggregates
Young's modulus	$E_m = 30\,000 \text{ MPa}$	$E_a = 60\,000 \text{ MPa}$
Poisson ratio	$\nu_m = 0.2$	$\nu_a = 0.2$

All simulations, comprising FOM and ROM, are carried out using a single core (Intel Core i7-10700) and serial implementations. It is noted that, the current implementation is not optimized and the provided numbers regarding computation time serve as a proof of concept rather than a rigorous comparison of the computational performance of both models.

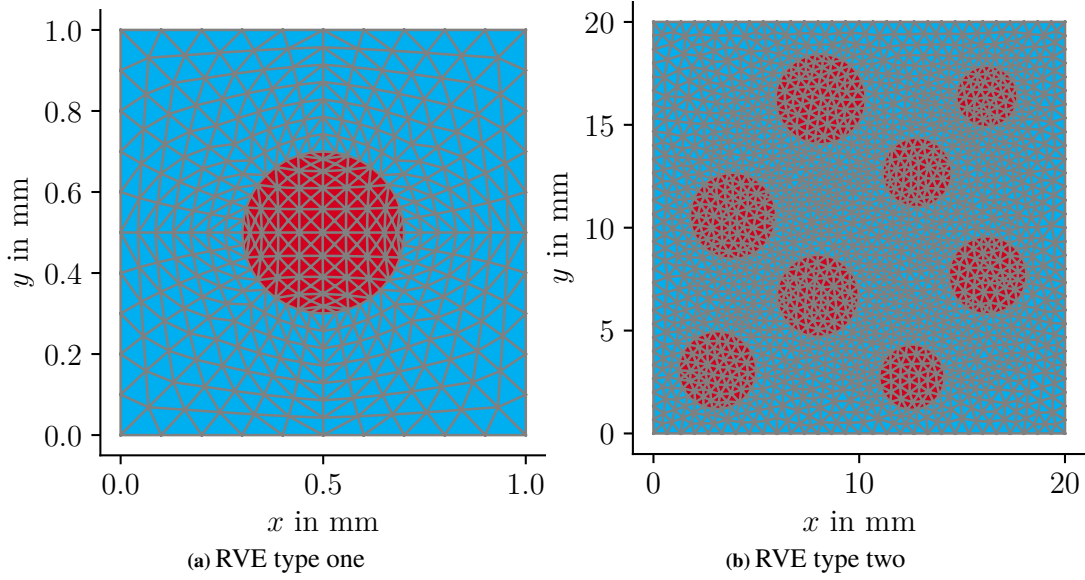


FIGURE 5 RVE types used in the examples.

#### 4.1 | Block example

In this example, eq. (1) is solved on a global domain  $\Omega_{\text{gl}} = (0, 5)^2$  with Dirichlet data on the boundary  $\Sigma_D := \partial\Omega_{\text{gl}}$  given in index notation by

$$u_i^D = a_{ij}x_j + b_{ij}x_j^2, \quad a_{ij}, b_{ij} \in \mathbb{R}. \quad (29)$$

An RVE of type one (fig. 5a) is used and, consequently, the coarse grid is chosen as a structured grid with five cells in each spatial direction. While the performance of the empirical basis is compared to the hierarchical basis, the discretization level of the RVE is controlled via the number of vertices per edge  $n_{\text{verts}}$ . Only a single oversampling problem with  $\Gamma_\mu := \partial\hat{\Omega}$  and the *delta* training set is considered for the construction of the empirical basis. There is thus the assumption that, in this particular problem, the deformation of any RVE can be well approximated by a single set of empirical basis functions. Note that the additional training due to Dirichlet boundary conditions is not necessary since  $u_i^D$  lies in the span of the basis  $\{\xi_i\}_{i=1}^n$ . The values to be prescribed can be computed by projection and boundary conditions can be applied to the global system of equations after assembly.

First, the maximum projection error over a *testing set* of size 20 is discussed. The samples are drawn randomly from  $\mathbb{P} = [-1, 1]^{16}$  and the snapshots  $\{s_j\}_{j=1}^{20}$  are the solutions of the oversampling problem restricted to the inner RVE domain. The maximum projection error

$$\max_j \left\| s_j - \sum_{k=1}^n (s_j, \xi_k)_{\mathbb{V}_i} \xi_k \right\|_{\mathbb{V}_i}, \quad (30)$$

is (empirically) shown to decay exponentially and faster in the case of the empirical basis compared to the hierarchical basis, see fig. 6 and fig. 7, respectively.

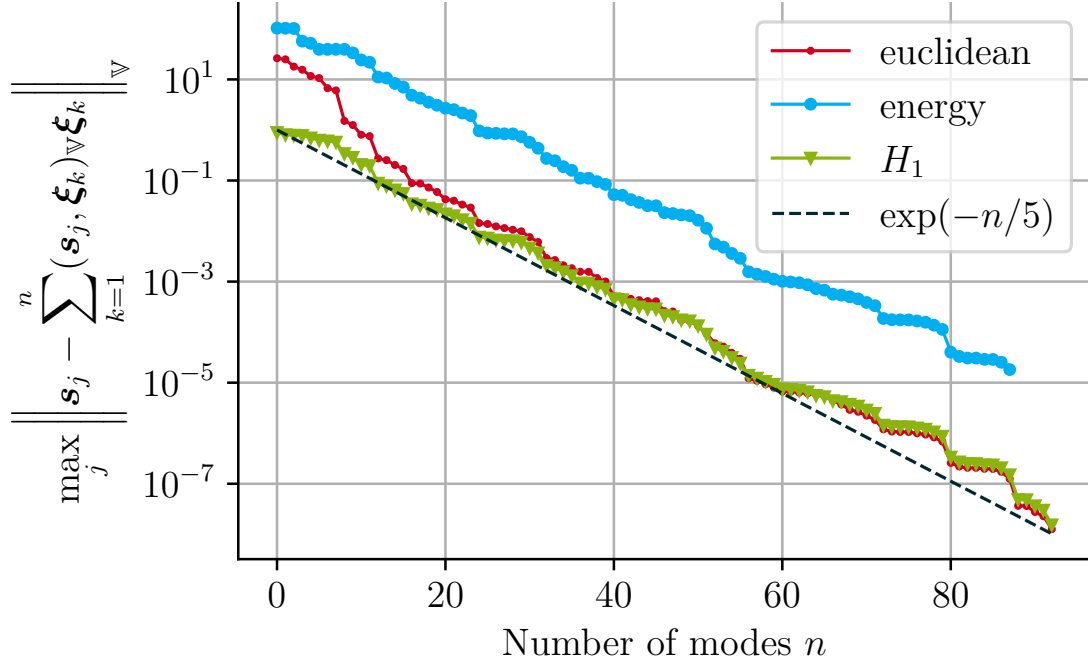


**FIGURE 6** Block example: projection error over a random testing set of size 20 in case of the empirical ( $\delta$ ) basis ( $n_{\text{verts}} = 21$ ) using different inner products.

Second, the global relative error with respect to the full order model is shown in figs. 8 and 9 for the empirical basis and hierarchical basis respectively. In both cases, the discretization of the RVE has no effect on the quality of the reduced order model relative to the FOM. However, the maximum number of basis functions per edge is limited by the discretization, as can be observed for  $n_{\text{verts}} = 3$  and  $n_{\text{verts}} = 5$ .

Furthermore, fig. 10 gives an impression of the solution and where the maximum error is located. In case of the empirical basis (fig. 10b), the maximum error is located at the boundary and edges perpendicular to the boundary. Although this is expected since RVEs on the boundary were not additionally trained, the overall error is still smaller compared to the hierarchical basis (fig. 10c). Here it is noted that, in general, we cannot expect the hierarchical basis to perform very well in the interior, but it is useful and preferred to model Dirichlet boundary conditions alleviating the need for additional training in case of the empirical basis. Consequently, for RVEs on the Dirichlet boundary of the global structure, we propose to use the hierarchical basis on edges  $\Gamma_e^i \subset \Sigma_D$ , while for the remaining edges the empirical basis should be used.

Finally, the reduction in computational cost is illustrated by the number of unknowns in the discrete equation system for both models. The finest discretization ( $n_{\text{verts}} = 11$ ) results in 76 402 DoFs in the case of the FOM, leading to a solution time of about nine seconds. Using for instance  $n_{\text{mpe}} = 10$  modes per edge for the fine scale basis leads to 672 DoFs and a solution time of less than one tenth of a second in the case of the ROM.

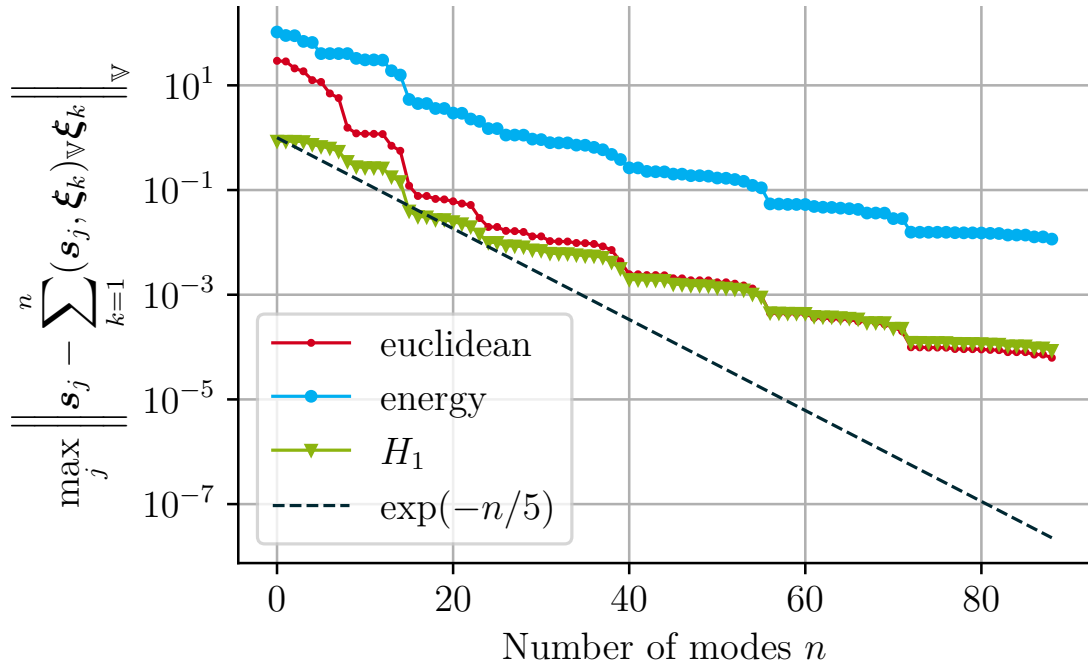


**FIGURE 7** Block example: projection error over a random testing set of size 20 in case of the hierarchical basis ( $n_{\text{verts}} = 21$ ) using different inner products.

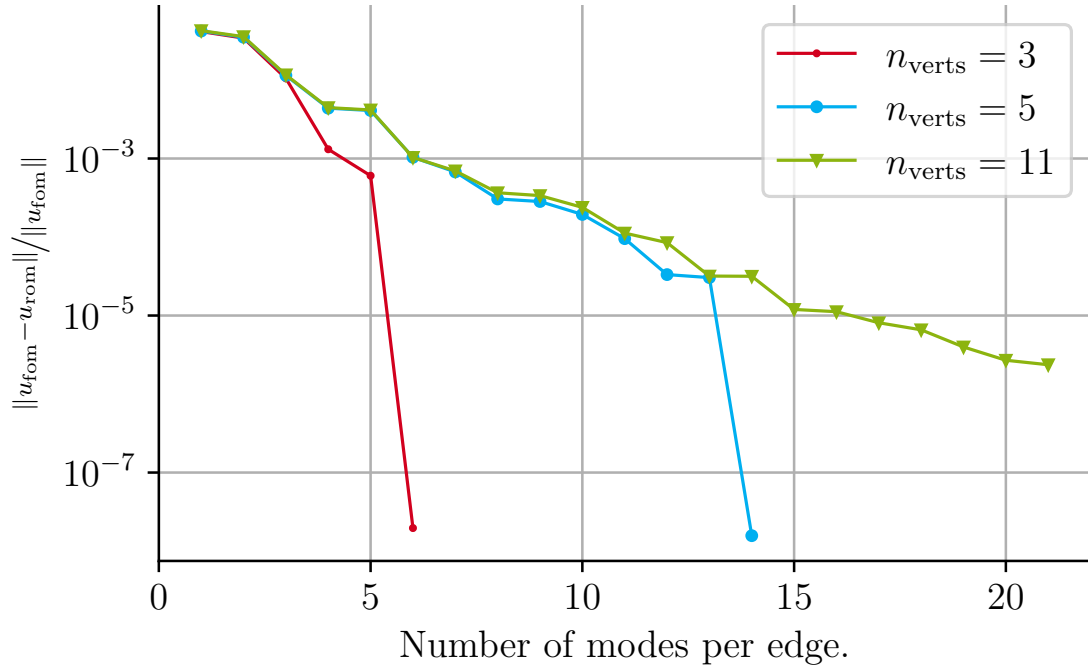


**FIGURE 8** Block example: relative error in energy norm for the empirical ( $\delta$ ) basis.



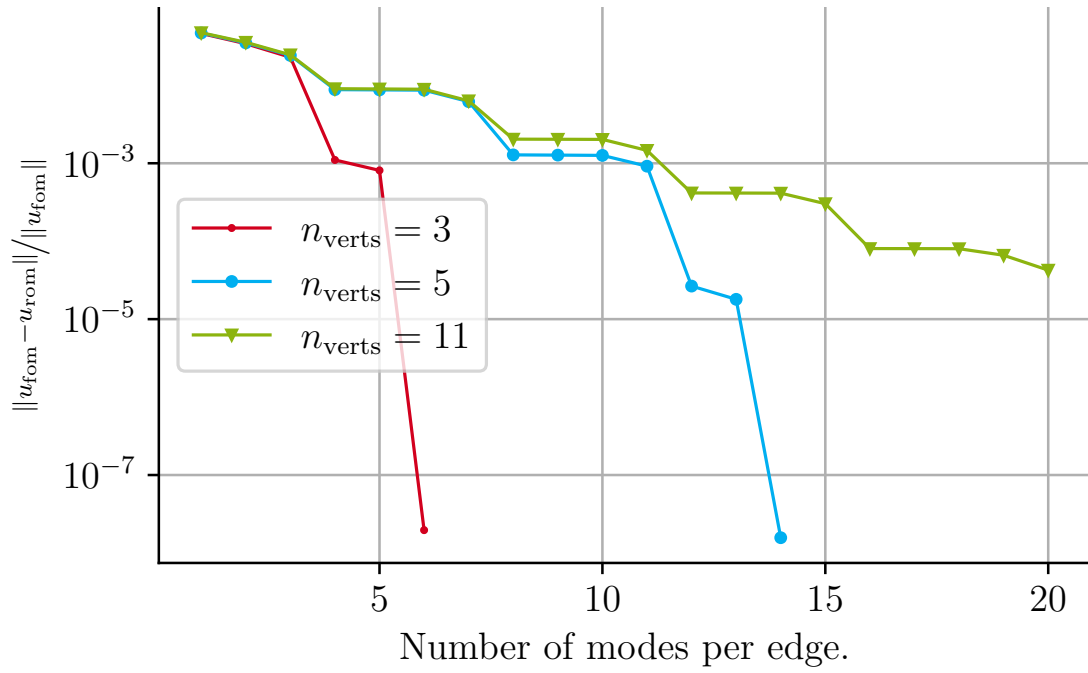


**FIGURE 9** Block example: relative error in energy norm for the hierarchical basis.

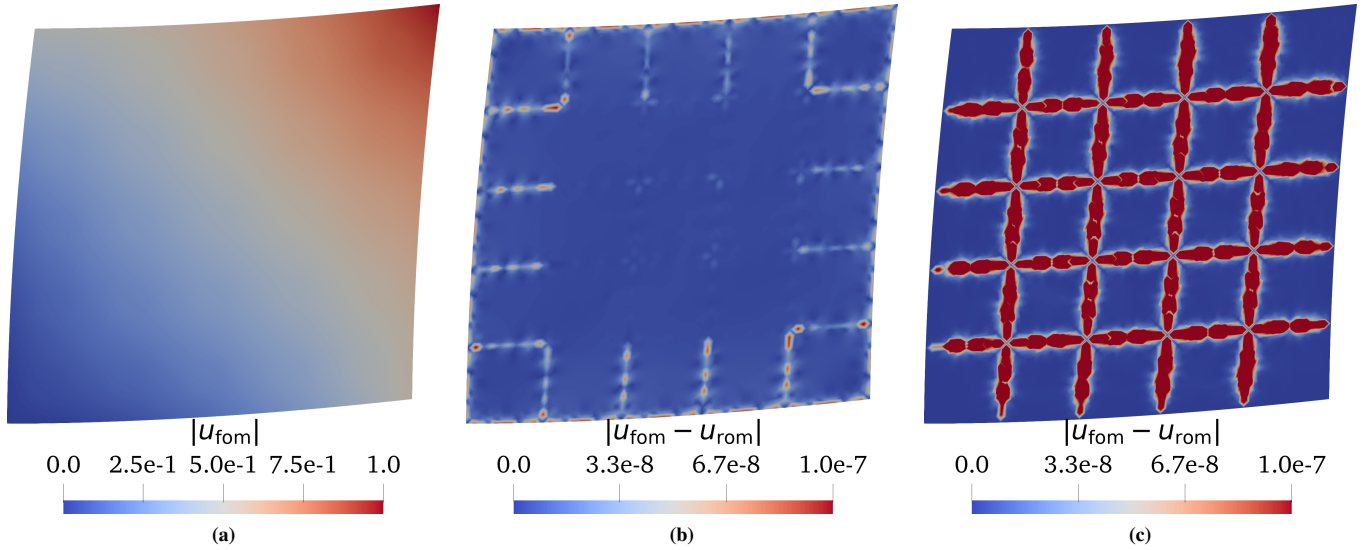


**FIGURE 10** (a) Magnitude of FOM solution, (b) ROM error in case of the empirical basis using 20 modes per edge and (c) ROM error in case of the hierarchical basis using 20 modes per edge in the deformed placement. In all cases a scale factor of 1 is used. In case of the absolute error the domain is scaled by the corresponding ROM solution.

## 4.2 | Beam example

A beam under the state of pure bending is considered on the domain  $\Omega_{gl} = (0, L) \times (0, c)$  as illustrated in fig. 11a. The bending moment  $M = 20c^2$  is distributed as  $f_x = \frac{240y}{c} - 120$ , such that the analytical solution (see<sup>40</sup>) in the case of a homogeneous isotropic and linear elastic material is

$$\sigma_{xx} = \frac{240y}{c} - 120, \quad \sigma_{yy} = \tau_{xy} = 0, \quad (31)$$

$$u = \left( \frac{240}{c}xy - 120x \right) \frac{1}{E}, \quad (32)$$

$$v = -\frac{\nu}{E} \left( \frac{120}{c}y^2 - 120y \right) - \frac{1}{E} \frac{120}{c}x^2. \quad (33)$$

Here, both the support on the left and the loading on the right are modelled by prescribing the analytical solution for the displacement with material parameters  $E = E_m$  and  $\nu = \nu_m$ . In this example, the empirical basis (*delta* training set) is compared to the hierarchical basis for varying ratio  $E_a/E_m$  of Young's moduli of the aggregates and matrix, as summarized in table 2. Furthermore, the empirical basis (*delta* training set) is compared to the empirical basis (*SoI* training set) in the case  $E_a/E_m = 2$ .

The dimensions of the beam  $L$  and  $c$  are chosen such that the coarse grid consists of  $50 \times 5$  RVEs of type two, see fig. 5b. Therefore, the configurations to be considered in the offline phase (see fig. 11b) are categorized as follows. Configuration 1 (gray, referred to as *inner*) is used to construct the empirical basis for all RVEs in the interior. The configurations 2, 4, 6 & 8 (red, referred to as *mixed*) are the cases in which one of the edges  $\Gamma_e^i$  of the subdomain of interest  $\Omega_i$  is part of the Neumann as well as the Dirichlet boundary. Accordingly, the configurations 3 & 7 (yellow, referred to as *hom Neumann*) and 5 & 9 (blue, referred to as *Dirichlet*) are the cases where  $\Gamma_e^i \subset \Sigma_N$  and  $\Gamma_e^i \subset \Sigma_D$  respectively. Actually, there are more configurations to consider, e. g. in the *transition zone* between configurations 2 and 9 (or 2 and 3 etc.). To illustrate this, the oversampling domains  $\hat{\Omega}_1, \hat{\Omega}_2, \dots, \hat{\Omega}_5$  with their respective subdomain of interest  $\Omega_i, i = 1, 2, \dots, 5$  are shown in fig. 12.  $\hat{\Omega}_1$  and  $\hat{\Omega}_5$  belong to the configurations 2 and 8, respectively and  $\hat{\Omega}_3$  is the oversampling domain for configuration 9. However, the configurations  $\hat{\Omega}_2$  and  $\hat{\Omega}_4$  are not trained additionally since the deformation of the bottom edge of  $\Omega_2$  is the same as the deformation of the top edge of  $\Omega_1$ . Also, the deformation of the top edge of  $\Omega_2$  is the same as the deformation of the bottom edge of  $\Omega_3$ . Thus, for the transition zone it is sufficient to add the snapshots of the top edge of  $\Omega_1$  to the bottom-top-snapshot-set in the *Dirichlet* configuration (number 9). It also follows that the basis generated from this data is to be set for the bottom and top edges of all RVE subdomains in

**TABLE 2** Scenarios studied in the beam example.

basis type	ratio $E_a/E_m$		
	1	1.5	2
empirical	scenario A	scenario B	scenario C
hierarchical	scenario D	scenario E	scenario F

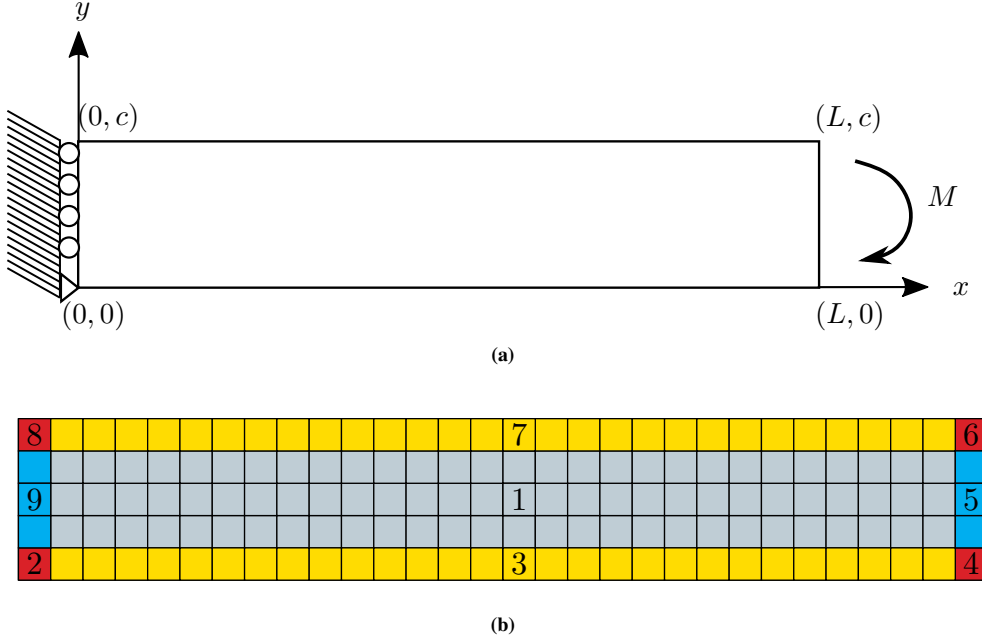


**FIGURE 11** Schematic representation (a) of the beam problem and coarse grid discretization showing configurations to be considered in the offline phase (b).

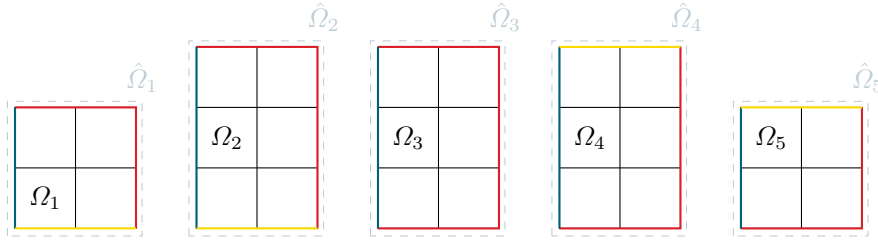


**FIGURE 12** The configurations of the oversampling domain  $\hat{\Omega}$  for the subdomains  $\Omega_1, \Omega_2, \dots, \Omega_5$  on the left Dirichlet boundary in case of the beam example. The colors indicate the boundaries  $\Sigma_D$  (blue),  $\Sigma_N$  (yellow) and  $\Gamma_\mu$  (red) whose topology is changing.

configuration 9 as well as for the top edge of  $\Omega_1$  and the bottom edge of  $\Omega_5$ . For the other transitions, we proceed in the same manner.

Furthermore, the Dirichlet boundary conditions can be realized either by setting the Dirichlet data directly as a basis function or by setting the hierarchical basis for edges  $\Gamma_e^i \subset \Sigma_D$ . Here, the hierarchical basis is set and the associated boundary values to be prescribed are computed via projection.

For varying ratio  $E_a/E_m$  of Young's moduli for the aggregates and matrix, the global relative error is shown in fig. 13. In the homogeneous case, i.e.  $E_a/E_m = 1$ , for the hierarchical basis it amounts to a nested finite element method and for the number of modes per edge  $n_{\text{mpe}} \geq 2$  the analytical solution can be represented exactly. However, for ratios  $E_a/E_m > 1$  the hierarchical basis does not yield a good approximation of the fine scale part of the displacement, whereas the relative error is already below

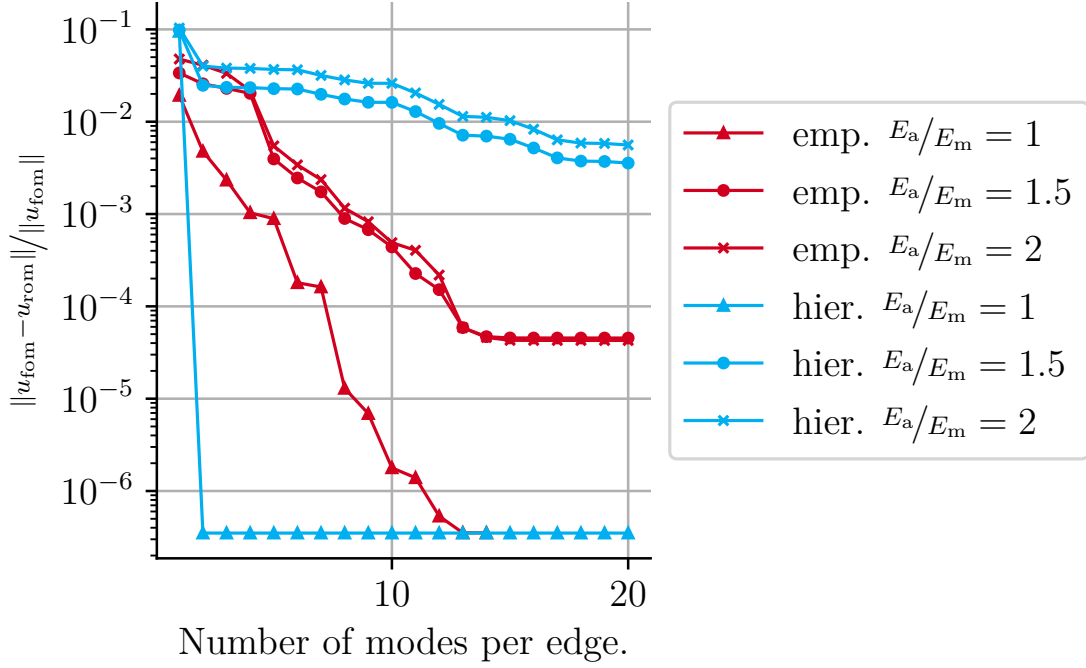


**FIGURE 13** Beam example: relative error in the energy norm against number of modes per edge. The empirical basis (*delta* training set) and hierarchical basis are compared for varying ratio of Young's moduli. The different scenarios are summarized in table 2.

$1 \cdot 10^{-3}$  for the empirical basis (*delta* training set) using 10 modes per edge. But, as the number of modes per edge is increased the global relative error stagnates. The reason for this is the reduction in the parameter space of the oversampling problem and the chosen *delta* training set, which leads to even less snapshot data in case of the *mixed* configurations due to the decreased size of the boundary  $\Gamma_\mu$ . Consequently, the maximum error is located at the Neumann boundary of these configurations which is shown in fig. 15b. Here also the absolute error using the hierarchical basis is shown for comparison (fig. 15c). Moreover, fig. 14 shows that despite the limitation in training data due to the *mixed* configurations, for the interior the error still decreases with increasing number of modes in the case of the *delta* training set. While the *SoI* approach yields a more rapid decay of the error, it is limited in terms of number of basis functions due to the similar training data (i.e. deformation states of the quadrilateral elements) in this particular case of pure bending.

In this example, the chosen coarse and fine grid discretizations leads to 3 678 602 DoFs for the FOM and 6 162 DoFs for the ROM when using  $n_{\text{mpe}} = 10$  modes per edge for the fine scale basis. While the FOM takes about three minutes, the ROM is completed in less than a second.

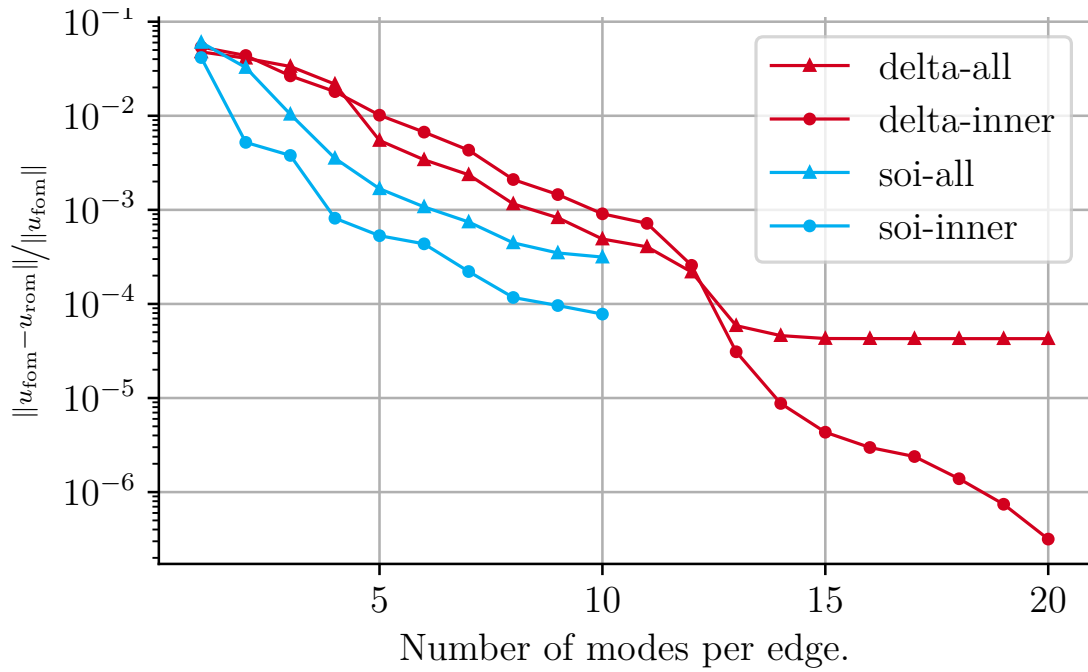


**FIGURE 14** Beam example: relative error in the energy norm against number of modes per edge and comparison of the *delta* and *SoI* training set for  $E_s/E_m = 2$ . The integration carried out over only the interior of the coarse grid (inner) is compared to the case where all coarse grid elements are taken into account (all).

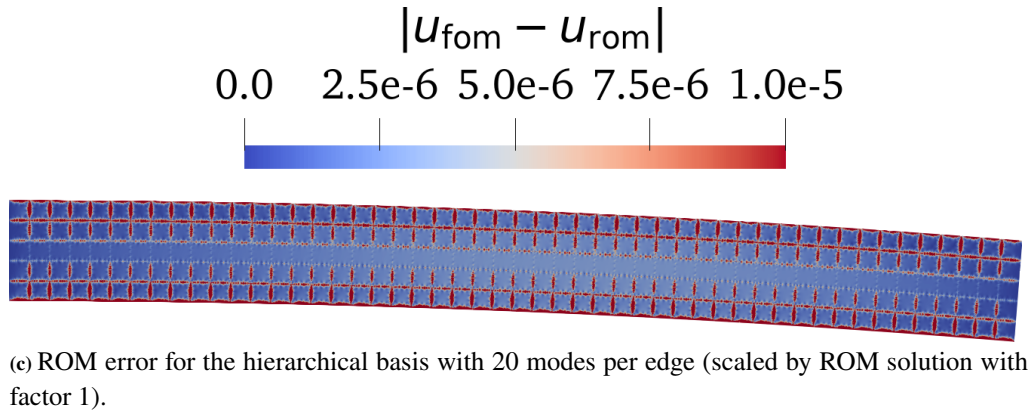
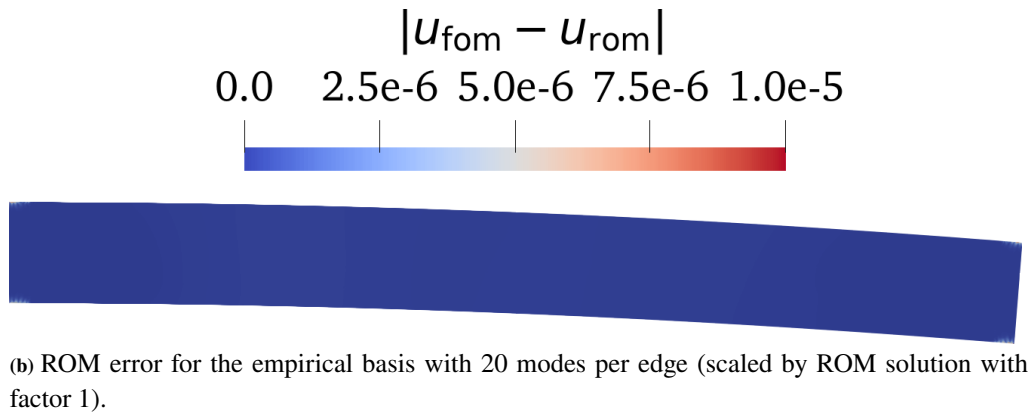
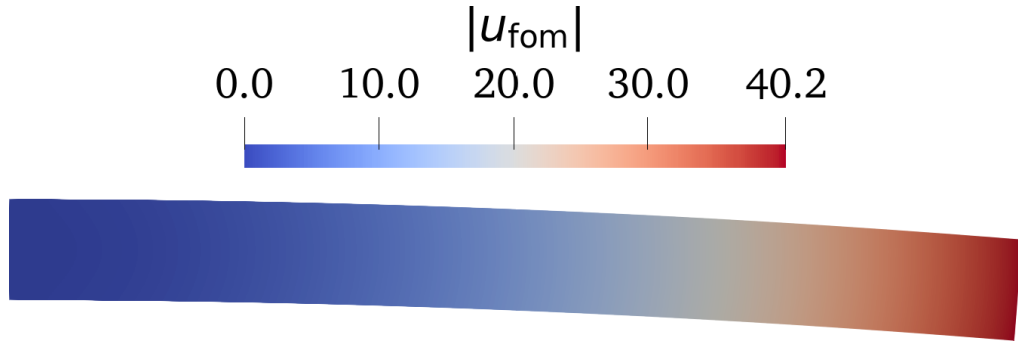


**FIGURE 15** Magnitude of the displacement solution (a) and absolute error (b, c) in the deformed placement for ratio of Young's moduli  $E_a/E_m = 2$ .

### 4.3 | L-panel example

The third example is an L-shaped panel, see fig. 16a. It features a more complex geometry as well as the point load implemented as a Neumann boundary condition. For simplicity, it is modeled as a linearly varying hat function with maximum value  $t_y = 200 \text{ N/mm}^2$  distributed over two coarse grid cells, such that the maximum vertical displacement is  $u_y \approx 5.4 \text{ mm}$ . Again RVE type two (see fig. 5b) is used leading to the coarse grid and configurations as shown in fig. 16b. The different configurations are encoded by color in the same manner as in the beam example (section 4.2), with the additional configurations 3 and 4 (green, referred to as *inhom Neumann*) marking inhomogeneous Neumann boundary conditions. To simplify the implementation, any transition zones are ignored in the sense that, for edges between neighbouring configurations the basis functions generated from the *interior* configuration are set. For example, for both the right edge of the RVE in configuration 9 and the left edge of the RVE in configuration 7, the basis functions of configuration 8 are set. In case of the L-Panel, the *delta* training set is compared to the *SoI* training set.

Similar to the beam example, the error decays with increasing number of modes per edge (see fig. 17), up to the point where the maximum number of modes per edge is reached for one of the configurations. Here, this is the case for the *inhom Neumann* configurations with at most 10 modes per edge. In contrast to the beam example, there is almost no difference between the two training sets. This is mainly due to the fact that the deformation states of the RVEs vary greatly over the whole structure and therefore in this case some type of clustering of the states in the training would be necessary to generate spaces specifically tailored for these states. Moreover, fig. 18 shows the absolute error between the FOM and the ROM for the L-panel. Again large errors are located at the Neumann boundary which limits the maximum number of modes. In addition, the maximum error occurs in the transition zone from the homogeneous Neumann boundary to the interior of the structure near the recessed corner which is known to be the critical area of the structure.

The chosen coarse and fine grid discretizations lead to 4 411 202 DoFs for the FOM and 7 082 DoFs for the ROM when using  $n_{\text{mpe}} = 10$  modes per edge for the fine scale basis. Using a single core, the FOM takes about three minutes while the ROM is evaluated within three seconds.

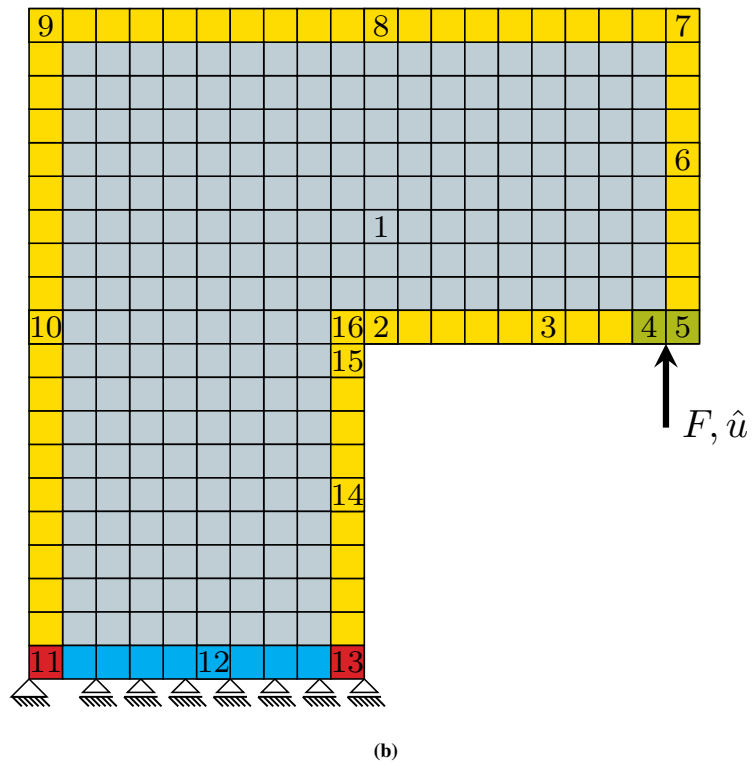
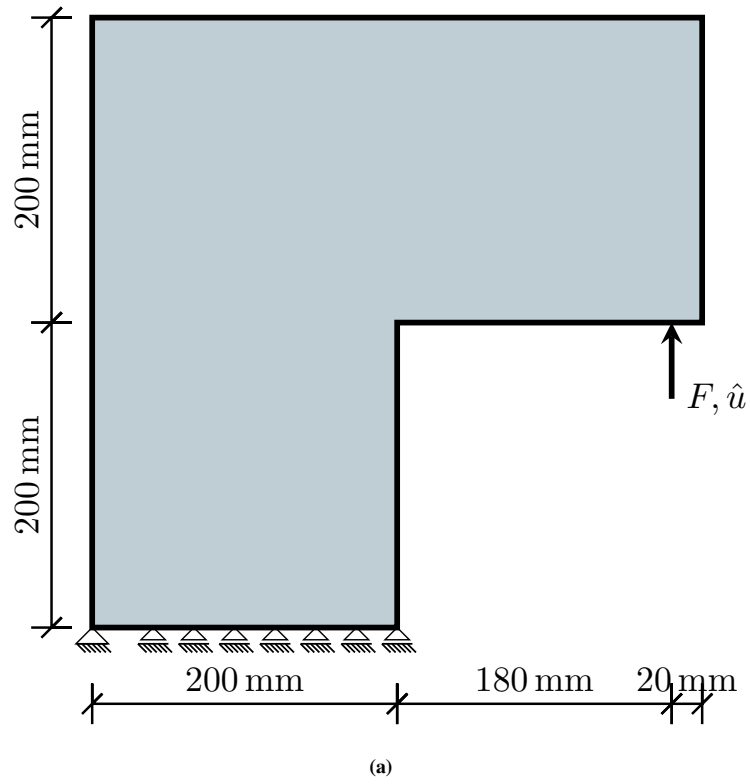


**FIGURE 16** Schematic representation (a) and different configurations present in the chosen coarse grid (b) of the L-Panel example.



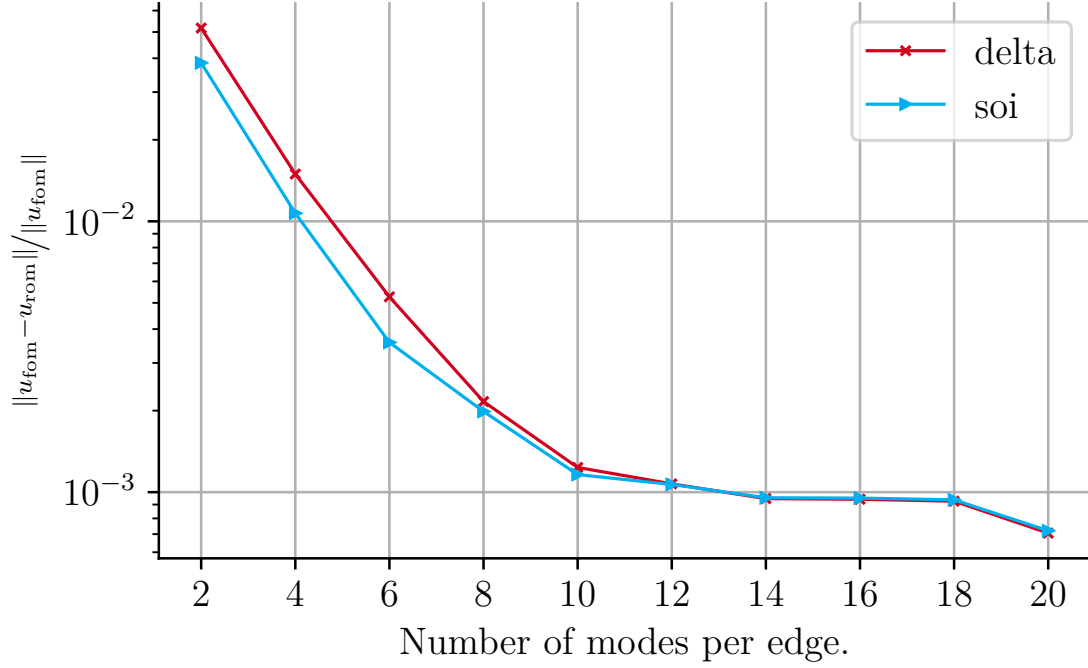


**FIGURE 17** L-Panel example: relative error in the energy norm against number of modes per edge.

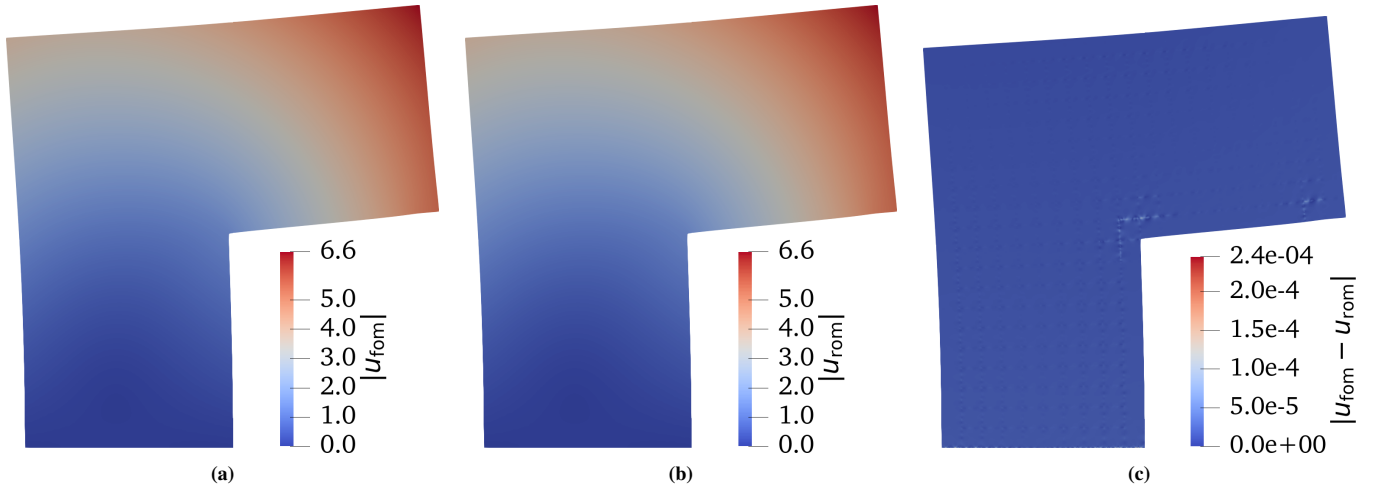


**FIGURE 18** Magnitude of the displacement solution for FOM (a) and ROM (b), both with a scale factor of 5. The ROM error (c) is shown in case of the empirical basis (*delta* training set) using 10 modes per edge.

## 5 | CONCLUSION

In this contribution, a methodology to model linear elastic heterogeneous structures is presented. A method combining the variational multiscale method, domain decomposition and model order reduction techniques is developed and applied to model the influence of the fine scale on the coarse scale directly. Herein, local approximation spaces for RVE subdomains are constructed

which allow for a conforming coupling in the framework of standard finite element assembly and hence an easy implementation. The resulting global system of equations is sparse and reduced in size compared to the full order model.

With regard to the online phase a minimum speedup of about 60 was obtained for the presented examples. Moreover, the approach features a reduction in the parameter space of the oversampling problem which greatly reduces the offline cost while yielding an accurate enough approximation of the global solution. The presented basis functions comprise a *hierarchical* and an *empirical* basis. While the performance of the empirical basis is generally superior, the realization of Dirichlet boundary conditions which do not lie in the span of the basis does not work well in this approach and thus the use of the hierarchical basis is suggested for the Dirichlet boundary. Furthermore, the chosen parametrization enables to incorporate physical states present in the analyzed structure into the training (*SoI training set*). In contrast to the *delta* training set with less physical meaningful parameter values, the decay in the relative error compared to the FOM is more rapid for the *SoI* basis, as shown in the beam example. However, currently only a single local subdomain space for the interior is constructed which is used throughout the interior of the entire structure. Regarding the L-shaped panel, this lessens the quality of the *SoI* basis as the training data covering all states present in the structure leads to a modest decay of the error similar to the *delta* basis. Possibly for a more efficient reduction, one would like to group the training data by means of clustering methods and analogously construct several local spaces, each tailored specifically to the displacement state of the respective cluster, for the interior of the structure.

Nevertheless, means to include physical states and their variation in the training data is thought to be promising in view of the extension of the method to the nonlinear case, which is subject of future work. In contrast to the linear case the choice of the correct amplitudes of the boundary data in the oversampling problem or amplitudes of the edge modes when extending these into the RVE subdomain poses a great challenge. Moreover, regarding the hyper-reduction methods referred to in section 1, usually a second projection subspace for the nonlinear term is needed. Furthermore, the choice of the snapshots for the second subspace — in the context of solid mechanics this is a subspace for the stresses — is not trivial and several approaches exist in the literature. Examples are the use of non-equilibrated snapshots of the Newton iteration<sup>41</sup> or the use of statically inadmissible stress approximations in addition to the equilibrated snapshots<sup>24</sup>.

## Acknowledgements

The authors gratefully acknowledge financial support by the German Research Foundation (DFG), project number 394350870, and by the European Research Council (ERC) under the European Union's Horizon 2020 research and innovation programme (ERC Grant agreement No. 818473).

## References

1. Miehe C, Koch A. Computational micro-to-macro transitions of discretized microstructures undergoing small strains. *Archive of Applied Mechanics (Ingenieur Archiv)* 2002; 72(4-5): 300-317. doi: 10.1007/s00419-002-0212-2
2. Feyel F, Chaboche JL. FE2 multiscale approach for modelling the elastoviscoplastic behaviour of long fibre SiC/Ti composite materials. *Computer Methods in Applied Mechanics and Engineering* 2000; 183(3-4): 309-330. doi: 10.1016/s0045-7825(99)00224-8
3. Geers M, Kouznetsova V, Brekelmans W. Computational homogenization. In: Pippan R, Gumbsch P., eds. *Multiscale Modelling of Plasticity and Fracture by Means of Dislocation Mechanics* Vienna: Springer Vienna. 2010 (pp. 327-394)
4. Geers M, Kouznetsova V, Brekelmans W. Multi-scale computational homogenization: Trends and challenges. *Journal of Computational and Applied Mathematics* 2010; 234(7): 2175-2182. doi: 10.1016/j.cam.2009.08.077
5. Nemat-Nasser S, Hori M. *Micromechanics: Overall Properties of Heterogeneous Materials*. Amsterdam: Elsevier. 1st ed. 1993.
6. Bishop J, Hill R. XLVI. A theory of the plastic distortion of a polycrystalline aggregate under combined stresses.. *The London, Edinburgh, and Dublin Philosophical Magazine and Journal of Science* 1951; 42(327): 414-427. doi: 10.1080/14786445108561065
7. Hill R. Elastic properties of reinforced solids: Some theoretical principles. *Journal of the Mechanics and Physics of Solids* 1963; 11(5): 357-372. doi: 10.1016/0022-5096(63)90036-x
8. Gitman I. *Representative volumes and multi-scale modelling of quasi-brittle materials*. dissertation. Technische Universiteit Delft, Delft, The Netherlands; 2006.
9. Gitman I, Askes H, Sluys L. Representative volume: Existence and size determination. *Engineering Fracture Mechanics* 2007; 74(16): 2518-2534. doi: 10.1016/j.engfracmech.2006.12.021
10. Hesthaven JS, Rozza G, Stamm B. *Certified Reduced Basis Methods for Parametrized Partial Differential Equations*. SpringerBriefs in Mathematics Springer International Publishing . 2016
11. Quarteroni A, Manzoni A, Negri F. *Reduced Basis Methods for Partial Differential Equations*. 92 of UNITEXT - La Matematica per il 3+2. Cham: Springer International Publishing . 2016
12. Prud'homme C, Rovas D, Veroy K, et al. Reliable Real-Time Solution of Parametrized Partial Differential Equations: Reduced-basis Output Bound Methods. *Journal of Fluids Engineering* 2001; 124(1): 70-80. doi: 10.1115/1.1448332

13. Veroy K, Prud'homme C, Rovas D, Patera AT. A Posteriori Error Bounds for Reduced-Basis Approximation of Parametrized Noncoercive and Nonlinear Elliptic Partial Differential Equations. In: AIAA. American Institute of Aeronautics and Astronautics; 2003: 2003-3847
14. Holmes P, Lumley JL, Berkooz G, Rowley CW. *Turbulence, Coherent Structures, Dynamical Systems and Symmetry*. Cambridge Monographs on Mechanics Cambridge University Press . 2009
15. Kunisch K, Volkwein S. Galerkin Proper Orthogonal Decomposition Methods for a General Equation in Fluid Dynamics. *SIAM Journal on Numerical Analysis* 2002; 40(2): 492-515. doi: 10.1137/s0036142900382612
16. Barrault M, Maday Y, Nguyen NC, Patera AT. An 'empirical interpolation' method: Application to efficient reduced-basis discretization of partial differential equations. *Comptes Rendus Mathematique* 2004; 339(9): 667-672. doi: 10.1016/j.crma.2004.08.006
17. Chaturantabut S, Sorensen DC. Nonlinear Model Reduction via Discrete Empirical Interpolation. *SIAM Journal on Scientific Computing* 2010; 32(5): 2737-2764. doi: 10.1137/090766498
18. Ryckelynck D. A priori hyperreduction method: An adaptive approach. *Journal of Computational Physics* 2005; 202(1): 346-366. doi: 10.1016/j.jcp.2004.07.015
19. Ryckelynck D. Hyper-reduction of mechanical models involving internal variables. *International Journal for Numerical Methods in Engineering* 2009; 77(1): 75-89. doi: 10.1002/nme.2406
20. Guo M, Hesthaven JS. Reduced order modeling for nonlinear structural analysis using Gaussian process regression. *Computer Methods in Applied Mechanics and Engineering* 2018; 341: 807-826. doi: 10.1016/j.cma.2018.07.017
21. Raissi M, Perdikaris P, Karniadakis G. Physics-informed neural networks: A deep learning framework for solving forward and inverse problems involving nonlinear partial differential equations. *Journal of Computational Physics* 2019; 378: 686-707. doi: 10.1016/j.jcp.2018.10.045
22. Yvonnet J, He QC. The reduced model multiscale method (R3M) for the non-linear homogenization of hyperelastic media at finite strains. *Journal of Computational Physics* 2007; 223(1): 341-368. doi: 10.1016/j.jcp.2006.09.019
23. Gouy O, Kerfriden P, Bordas S. Bridging analytical and computational homogenisation for nonlinear multiscale problems: A reduced order modelling approach for a damage problem. tech. rep., Cardiff University, School of Engineering; Cardiff, UK: 2014.

24. Hernández J, Oliver J, Huespe A, Caicedo M, Cante J. High-performance model reduction techniques in computational multiscale homogenization. *Computer Methods in Applied Mechanics and Engineering* 2014; 276: 149-189. doi: 10.1016/j.cma.2014.03.011
25. Buhr A, Iapichino L, Ohlberger M, Rave S, Schindler F, Smetana K. Localized model reduction for parameterized problems. <http://arxiv.org/abs/1902.08300>; 2019.
26. Babuska I, Lipton R. Optimal Local Approximation Spaces for Generalized Finite Element Methods with Application to Multiscale Problems. *Multiscale Modeling & Simulation* 2011; 9(1): 373-406. doi: 10.1137/100791051
27. Smetana K, Patera AT. Optimal Local Approximation Spaces for Component-Based Static Condensation Procedures. *SIAM Journal on Scientific Computing* 2016; 38(5): A3318-A3356. doi: 10.1137/15m1009603
28. Hou TY, Wu XH. A Multiscale Finite Element Method for Elliptic Problems in Composite Materials and Porous Media. *Journal of Computational Physics* 1997; 134(1): 169-189. doi: 10.1006/jcph.1997.5682
29. Buhr A, Smetana K. Randomized Local Model Order Reduction. *SIAM Journal on Scientific Computing* 2018; 40(4): A2120-A2151. doi: 10.1137/17m1138480
30. Taddei T, Patera AT. A Localization Strategy for Data Assimilation; Application to State Estimation and Parameter Estimation. *SIAM Journal on Scientific Computing* 2018; 40(2): B611-B636. doi: 10.1137/17m1116830
31. Hughes TJ, Feijóo GR, Mazzei L, Quincy JB. The variational multiscale method—a paradigm for computational mechanics. *Computer Methods in Applied Mechanics and Engineering* 1998; 166(1-2): 3-24. doi: 10.1016/s0045-7825(98)00079-6
32. Arbogast T, Boyd KJ. Subgrid Upscaling and Mixed Multiscale Finite Elements. *SIAM Journal on Numerical Analysis* 2006; 44(3): 1150-1171. doi: 10.1137/050631811
33. Fish J, Shek K. Multiscale analysis of large scale nonlinear structures and materials. *International Journal for Computational Civil and Structural Engineering* 2000; 1: 79-90.
34. Hund A, Ramm E. Locality constraints within multiscale model for non-linear material behaviour. *International Journal for Numerical Methods in Engineering* 2007; 70(13): 1613-1632. doi: 10.1002/nme.1953
35. Bertram A, Glüge R. *Solid Mechanics*. Springer International Publishing . 2015
36. Zienkiewicz O, Taylor R. *The Finite Element Method Volume 1: The Basis*. Oxford: Butterworth-Heinemann. 5th ed. 2000.
37. Milk R, Rave S, Schindler F. pyMOR – Generic Algorithms and Interfaces for Model Order Reduction. *SIAM Journal on Scientific Computing* 2016; 38(5): S194-S216. doi: 10.1137/15m1026614

38. Sirovich L. Turbulence and the dynamics of coherent structures. I. Coherent structures. *Quarterly of Applied Mathematics* 1987; 45(3): 561-571. doi: 10.1090/qam/910462
39. Unger JF, Eckardt S. Multiscale Modeling of Concrete. *Archives of Computational Methods in Engineering* 2011; 18(3): 341-393. doi: 10.1007/s11831-011-9063-8
40. Lee NS, Bathe KJ. Effects of element distortions on the performance of isoparametric elements. *International Journal for Numerical Methods in Engineering* 1993; 36(20): 3553-3576. doi: 10.1002/nme.1620362009
41. Amsallem D, Zahr MJ, Farhat C. Nonlinear model order reduction based on local reduced-order bases. *International Journal for Numerical Methods in Engineering* 2012; 92(10): 891-916. doi: 10.1002/nme.4371

**How to cite this article:** P. Diercks, K. Veroy, A. Robens-Radermacher, and J. F. Unger (2021), Multiscale modeling of linear elastic heterogeneous structures based on a localized model order reduction approach, *International Journal for Numerical Methods in Engineering*, submitted 2021.